JPhys Photonics

PAPER • OPEN ACCESS

Dynamic control of spontaneous emission using magnetized InSb higher-order-mode antennas

To cite this article: Sina Aghili *et al* 2024 *J. Phys. Photonics* **6** 035011

IOP Publishing J. Phys. Photonics 6 (2024) 035011 https://doi.org/10.1088/2515-7647/ad4c34

Journal of Physics: Photonics

CrossMark

OPEN ACCESS

RECEIVED
25 January 2024

REVISED
24 April 2024

ACCEPTED FOR PUBLICATION
15 May 2024

PUBLISHED
28 May 2024

PAPER

Dynamic control of spontaneous emission using magnetized InSb higher-order-mode antennas

Sina Aghili[1], Rasoul Alaee[2,3,*], Amirreza Ahmadnejad[4], Ehsan Mobini[2], Mohammadreza Mohammadpour[2], Carsten Rockstuhl[3,5] and Ksenia Dolgaleva[1,2]

[1] School of Electrical Engineering and Computer Science, University of Ottawa, Ottawa, Ontario K1N 6N5, Canada
[2] Department of Physics, University of Ottawa, Ottawa, Ontario K1N 6N5, Canada
[3] Karlsruhe Institute of Technology, Institute of Theoretical Solid State Physics, D-76131 Karlsruhe, Germany
[4] Department of Electrical Engineering, Sharif University of Technology, Tehran 11155-4365, Iran
[5] Institute of Nanotechnology, Karlsruhe Institute of Technology, D-76344 Eggenstein-Leopoldshafen, Germany
[*] Author to whom any correspondence should be addressed.

E-mail: rasoul.alaee@gmail.com

Keywords: active antenna, indium antimonide (InSb), local density of states, multipole moments, radiative decay rate, Zeeman-splitting effect, III-V semiconductors

Supplementary material for this article is available online

Abstract

We exploit InSb's magnetic-induced optical properties to design THz sub-wavelength antennas that actively tune the radiative decay rates of dipole emitters at their proximity. The proposed designs include a spherical InSb antenna and a cylindrical Si-InSb hybrid antenna demonstrating distinct behaviors. The former dramatically enhances both radiative and non-radiative decay rates in the epsilon-near-zero region due to the dominant contribution of the Zeeman-splitting electric octupole mode. The latter realizes significant radiative decay rate enhancement via magnetic octupole mode, mitigating the quenching process and accelerating the photon production rate. A deep-learning-based optimization of emitter positioning further enhances the quantum efficiency of the proposed hybrid system. These novel mechanisms are promising for tunable THz single-photon sources in integrated quantum networks.

1. Introduction

It has been long appreciated that the local density of states (LDOS), as seen by a quantum emitter, can be altered in a structured electromagnetic environment [1, 2]. The spontaneous emission (SE) rate and transition dipole strength, as the functional characteristics of a quantum emitter, greatly rely on LDOS variations [3]. In simple terms, the electric or magnetic dipole transition of quantum emitters, when considered as two-level systems, can couple to photonic resonances. Then, the enhancement of the LDOS, thanks to the structured photonic environment, accelerates the spontaneous transition rates of the quantum emitter. The SE rate enhancement is of great interest to diverse applications, including quantum source emission engineering [4–6], ultra-brighter optoelectronic devices [7–10], enhanced light–matter interaction for fluorescence spectroscopy [11–13], and single-photon sources (SPSs) [14–16].

Optical resonators are high-potential devices that can serve as the structured electromagnetic media for quantum emitters by providing an enhanced LDOS [17, 18]. Radiative coupling channels emerge in a coupled emitter-resonator system, allowing one to improve the SE rate of the quantum emitter. Microcavities [19], photonic crystals, and hyperbolic metamaterials [20–22] have been extensively explored as closed-cavity platforms with the potential to enhance the SE rate of quantum emitters significantly. In recent decades, optical antennas have been the subject of this extensive research. Optical antennas are open resonators composed of sub-wavelength dielectric or metallic elements that transfer the energy of their resonance modes to quantum emitters via radiative and non-radiative channels [23–25]. Enhanced light–matter interaction at the deep sub-wavelength scale is the distinguishing advantage of antennas over cavities. This leads to LDOS enhancement of quantum emitters in the coupled emitter-antenna systems. In this direction, metallic antennas enable one to modify the SE rate of quantum emitters due to the high near-field enhancement attained by localized surface plasmon resonances (LSPRs) [26–30]. Metallic nanorods [31] and ring resonators [32] are highly effective plasmonic sub-wavelength antennas for enhancing the SE rate of quantum emitters through the excitation of LSPRs, including transversal and longitudinal plasmonic modes in nanorods, and concurrent electric and magnetic resonant modes in ring resonators. In general, coupled emitter-plasmonic antenna systems usually introduce dominant non-radiative channels due to high Joule heating losses of metallic building blocks, resulting in low quantum efficiency for the coupled systems.

Alternative designs have been investigated to mitigate dissipation losses of plasmonic antennas. Interestingly, it was shown that plasmonic devices using a dielectric spacer could avoid or limit non-radiative decay channels [33]. This idea has flourished by employing dielectric optical antennas in a wide range of applications such as surface-enhanced Raman spectroscopy [34], surface-enhanced fluorescence [35], directional light emission [36], nonlinear processes [37], and Huygens sources [38]. Furthermore, optically induced electric and magnetic Mie resonances make high-index dielectric antennas capable of efficiently engineering the SE rate of quantum emitters with electric or magnetic transition dipole moment [39–42]. Besides the coexistence of electric and magnetic multipolar resonances at the sub-wavelength scale, unique characteristics such as negligible inherent losses and comparable near-field enhancement with metallic analogs enable high-index dielectric structures to suppress non-radiative channels and robustify radiative channels in the coupled emitter-dielectric antenna systems. Concentric hollow structures [43], Yagi-Uda designs [44], dimers [45], and oligomers [46] have been numerically and experimentally investigated to use the high potential of dielectric sub-wavelength antennas in engineering the SE rate of quantum emitters.

Among the reported cases exploited to control the SE rate of quantum emitters for specific applications, the research has been mostly limited to passive approaches such as design, material, and shape to improve the efficiency of the coupled emitter-photonic systems. Here, we aim to employ active antennas to dynamically control the SE or radiative decay rate of quantum emitters near the proposed antennas. By applying an external static magnetic field, we dynamically tune the scattering response of an optical antenna, leading to the radiative decay rate variations of a quantum emitter. In this respect, we need a material whose optical properties can be modulated upon magnetization [47]. Hence, indium antimonide (InSb), a III-V semiconductor with unique features of nonreciprocity, magnetoplasmonics, and magnetic tunability in the THz region [48–50], has been exploited to achieve an active sub-wavelength antenna. Without a static magnetic field, the scattering response of a spherical InSb antenna is divided into plasmonic, epsilon-near-zero (ENZ), and dielectric regions. By placing an electric dipole (ED) source close to the antenna as the quantum emitter, we observe different types of electromagnetic behaviors in the coupled emitter-antenna system. Non-radiative channels dominate the plasmonic region due to inherent losses of InSb below the plasma frequency, resulting in the quenching process. A transparency window corresponds to the ENZ region; hence, the quantum emitter does not experience the impact of the antenna. The coexistence of electric and magnetic multipolar resonances is observed in the dielectric region, leading to SE rate enhancement associated with dominant radiative channels. In the presence of the static magnetic field, the scattering characteristics of the InSb antenna are dramatically changed. The quenching effect becomes much more intense in the plasmonic region. Therefore, the radiative decay rate is negligible compared to the non-radiative one. The ENZ region completely disappears due to the Zeeman-splitting effect of plasmonic modes, and the quantum emitter experiences considerable radiative decay rate variations compared to the unmagnetized case. Despite dynamic control of the emission characteristics of the ED emitter via the magnetized InSb antenna, dominant non-radiative processes degrade the efficiency of the proposed antenna across the studied spectral range. To solve this limitation, as the next step, a hybrid dielectric antenna composed of Silicon (Si) and InSb layers has been proposed to serve as the high-index dielectric antenna, leading to a high radiative decay rate enhancement for the coupled magnetic dipole (MD) and ED emitter-antenna systems. Dual-band SE rate enhancement, robust magnetic response, and high quantum efficiency are important advantages realized by the magnetized hybrid antenna, opening up a possibility for the emergence of tunable magnetic SPSs.

2. Methodology

The spontaneous decay of a two-level system, the so-called quantum emitter, is a radiating process at a quantum level that can be estimated by Fermi's golden rule [51]. When we consider the interaction of quantum emitters with optical antennas as open resonators and lossy media, the normalized total decay rate ($\Gamma_{\mathrm{tot}}/\Gamma_0$) must be defined by LDOS in the form of [51]

$$\frac{\Gamma_{\mathrm{tot}}}{\Gamma_0} = \frac{\rho_n(\boldsymbol{r}_0,\omega)}{\rho_0(\boldsymbol{r}_0,\omega)} = \frac{\boldsymbol{n}_{\boldsymbol{p}}^{\boldsymbol{T}}\,\mathrm{Im}\left[\overleftrightarrow{\boldsymbol{G}}_s(\boldsymbol{r}_0,\boldsymbol{r}_0;\omega) + \overleftrightarrow{\boldsymbol{G}}_0(\boldsymbol{r}_0,\boldsymbol{r}_0;\omega)\right]\boldsymbol{n}_{\boldsymbol{p}}}{\boldsymbol{n}_{\boldsymbol{p}}^{\boldsymbol{T}}\,\mathrm{Im}\left[\overleftrightarrow{\boldsymbol{G}}_0(\boldsymbol{r}_0,\boldsymbol{r}_0;\omega)\right]\boldsymbol{n}_{\boldsymbol{p}}}, \tag{1}$$

where $\rho_n(\boldsymbol{r}_0,\omega)$ and $\rho_0(\boldsymbol{r}_0,\omega)$ represent the LDOS at the position $\boldsymbol{r}_0$ of the quantum emitter with a transition frequency ω in the presence and absence of the optical sub-wavelength antenna, respectively. The LDOS at the position of the quantum emitter is computed using the imaginary part of the Green function [23], and $\boldsymbol{n}_{\boldsymbol{p}}$ indicates the polarization's unit vector. Without the antenna, the LDOS only depends on the electromagnetic field generated by the quantum emitter ($\overleftrightarrow{\boldsymbol{G}_0}(\boldsymbol{r}_0,\boldsymbol{r}_0;\omega)$) at its position. Besides the self-generated field, in the presence of the antenna, the LDOS has another contribution from the electromagnetic field scattered by the antenna ($\overleftrightarrow{\boldsymbol{G}_s}(\boldsymbol{r}_0,\boldsymbol{r}_0;\omega)$) at the emitter position, showing the impact of the local field provided by optical sub-wavelength antennas on the total decay rate modification. The contribution of the LDOS to engineering the decay rates of a quantum emitter is a common point of classical and quantum electrodynamics [51]. From a classical point of view, a quantum emitter can be modeled by a point-like dipole as an oscillating current source located near an antenna. Both electrodynamical and classical approaches agree when the intrinsic quantum yield of the point-like quantum source is unity. The total decay rate is defined as the ratio of the total emitted power of a dipole source in the presence of the antenna to its total emitted power in the absence of the antenna in the form of

$$\frac{\Gamma_{\mathrm{tot}}}{\Gamma_0} = \frac{\Gamma_{\mathrm{r}} + \Gamma_{\mathrm{nr}}}{\Gamma_0} = \frac{P_{\mathrm{r}} + P_{\mathrm{nr}}}{P_0}, \tag{2}$$

where the radiative and non-radiative decay rates are denoted by Γ_{r} and Γ_{nr}, respectively. Here, P_{r} and P_{nr} are also the scattered and absorbed powers by the antenna, respectively. The part of the total power incident on the antenna decays into the non-radiative channels due to the inherent losses of the antenna [23, 51]. The remaining fraction of the radiation escapes from the coupled emitter-antenna system to free space as far-field radiation. It is thus necessary to calculate the corresponding powers represented in equation (2) using the Poynting theorem [52]. The total emitted power is obtained by integrating the Poynting vector flux over a surface enclosing the dipole source without the antenna. The far-field radiation of the coupled emitter-antenna system is computed by placing a Poynting vector surface integral around the entire system. The dissipated power is proportional to the power loss density, determined by a volume integral around the antenna.

In this study, we use COMSOL Multiphysics RF module package 6 to numerically compute the coupled emitter-antenna system's power rates corresponding to the dipole source's total decay rate [53, 54]. Owing to the inherent duality in classical electrodynamics, particularly in Maxwell's equations, the far-field radiation patterns of a quantum emitter possessing a transition magnetic dipole (MD) moment are indistinguishable from those with an ED moment. Consequently, the same numerical Poynting theorem applicable to EDs can be employed within COMSOL's RF module to compute the total decay rate of an MD emitter. The distinction lies in the necessity to define a point source with a transition MD moment within the simulation model.

3. Results

3.1. Spherical InSb antenna

The primary purpose of this study is to investigate how a static magnetic field applied to an optical antenna dynamically modifies the radiative decay rate of a dipole emitter in the weak-coupling regime. We first consider a spherical InSb antenna embedded in free space to serve as a sub-wavelength THz antenna. The antenna's radius is set to 30 μm, corresponding to the operation frequency range of 1.2–3 THz, matching the range of InSb's plasma frequency. The antenna's geometry and spectral range are chosen such that the antenna can support multipolar electromagnetic resonance modes. Upon magnetic excitation perpendicular to the incidence plane, the dielectric permittivity of InSb becomes anisotropic. It enables the Zeeman-splitting effects on the electronic energy levels of the material proportional to the cyclotron frequency of $\omega_c = eB/m^*$ depending on the external magnetic field (B), electron charge (e) and effective mass of the n-doped InSb ($m^* = 0.0142\,m_0$). The applied magnetic field strength is $B = 0.2$ T, a threshold

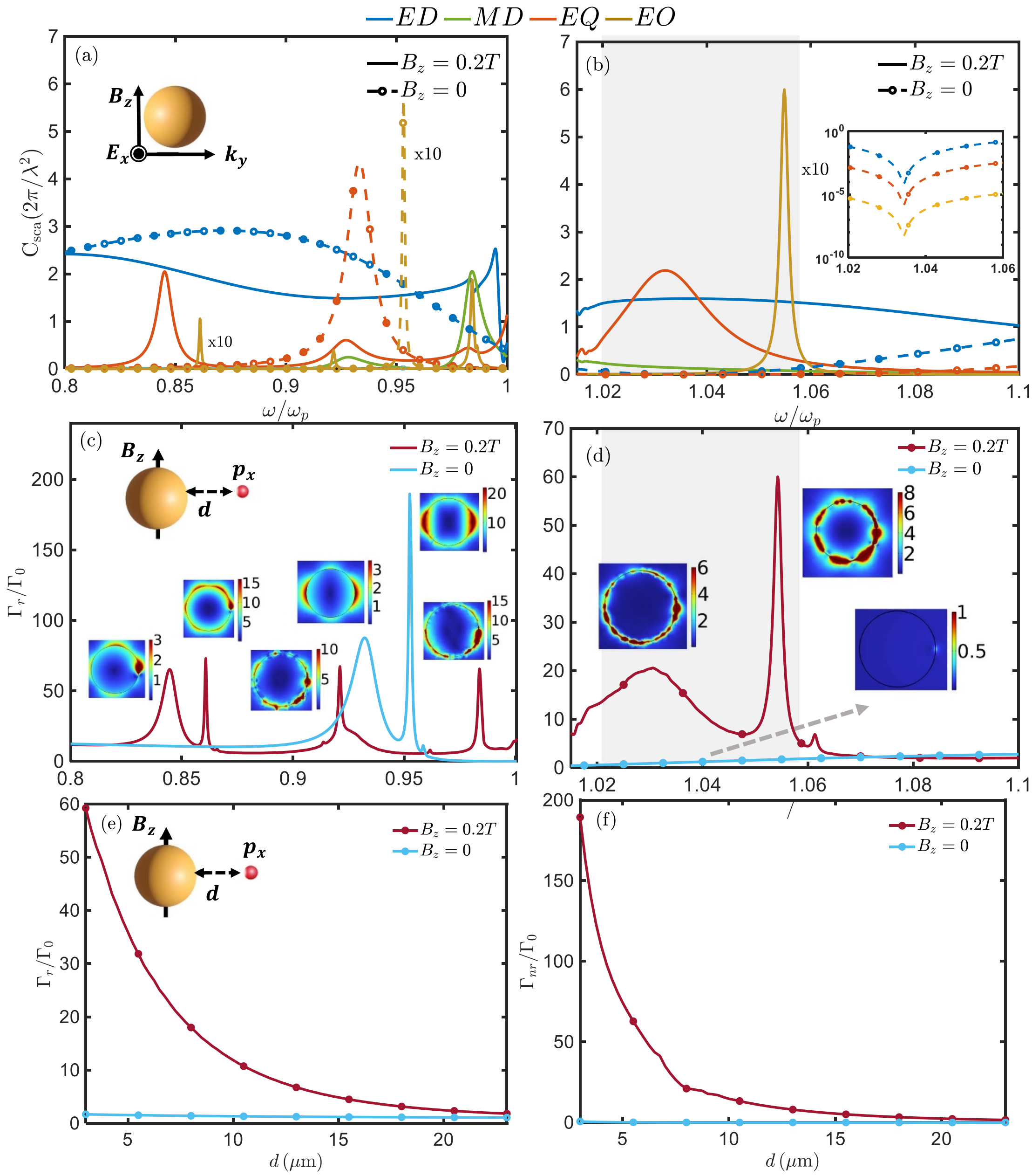

Figure 1. (a) and (b) The comparison of SCS spectra of the spherical InSb antenna in the static magnetic field's presence (solid lines) and absence (dashed lines). The external magnetic field ($B_z = 0.2$ T) is applied along the z-direction to dynamically modify the scattering characteristics of the antenna in the plasmonic (a) and ENZ (b) regions. (c) and (d) The spectral features of the radiative decay rate of the x-oriented ED source, which is placed at a distance of $d = 3\ \mu$m from the antenna. (c) For frequencies lower than ω_p, the coupled system realizes an enhanced multi-band radiative decay rate upon magnetization, while the unmagnetized case demonstrates a larger enhancement factor in a single band. (d) Due to the presence of Zeeman-splitting resonances, the radiative decay rate significantly improves in the ENZ region, highlighted by the gray area. The insets are the normalized electric field distributions around the coupled emitter-antenna system, displaying how the ED source excites electric resonant modes of the antenna through the radiative coupling channels. Variations of the radiative (e) and non-radiative (f) decay rates as a function of coupling distance (d) at the fixed frequency of $\omega/\omega_p = 1.05$.

value ensuring the Zeeman-splitting effect in the InSb semiconductor. Márquez and Sirvent [55]. (See supporting information for more detail.)

To gain insight into the light interaction with InSb semiconductor, we evaluate the scattering characteristics of the proposed antenna using multipolar decomposition [56]. We consider a linearly x-polarized plane wave with the wave vector **k** propagating along the y-direction (the illumination direction). By applying a static magnetic field along the z-direction, we induce anisotropy in the dielectric permittivity of InSb, thereby dynamically modifying the scattered light characteristics (see figure S1).

As shown in figure 1(a), the magnetically induced anisotropy lifts the mode degeneracy, leading to separated plasmonic resonances in the magnetized InSb antenna at frequencies lower than and around ω_p. The Zeeman-splitting effect results in new resonant modes whose spectral positions can be predicted [55].

The splits in atomic energy levels are linearly proportional to the Bohr magneton in the presence of weak magnetic fields. In the presence of the magnetic field $B_z = 0.2$ T, a narrow linewidth electric octupole (EO) resonance at $\omega/\omega_p = 0.951$ splits into multi-band EO resonances, where a peak at $\omega/\omega_p = 1.055$ considerably amplifies the antenna's scattering response. The magnitudes of the EO resonances have been multiplied by ten to emphasize their critical role in the radiated power, as shown in figures 1(a) and (b). A parent electric quadrupole (EQ) mode at $\omega/\omega_p = 0.94$ is split into two distinct EQ resonances at $\omega_{-,\mathrm{EQ}}/\omega_p = 0.84$ and $\omega_{+,\mathrm{EQ}}/\omega_p = 1.035$. Moreover, a broad ED mode is also split into resonances at $\omega_{-,\mathrm{ED}}/\omega_p = 0.8$ and $\omega_{+,\mathrm{ED}}/\omega_p = 0.99$. Contrary to the unmagnetized scenario, when an applied magnetic field couples with localized surface plasmon resonances, it can excite magneto-plasmonic modes. This results in the contribution of MD resonances to the antenna's spectral response, as depicted in figures 1(a) and (b).

The unmagnetized InSb antenna also experiences a plasmonic to ENZ transition response at frequencies slightly higher than ω_p. This electromagnetic behavior provides invisibility, highlighted by a gray box in figure 1(b). The inset depicts the minimum contributions of the multipoles, leading to an almost negligible scattering response, rendering the antenna nearly invisible. In the presence of the magnetic field $B_z = 0.2$ T, the electromagnetic response of the antenna supports a strong splitting of the EQ mode at $\omega/\omega_p = 1.035$ and a high-Q EO mode at $\omega/\omega_p = 1.055$, leading to a transition from invisibility to visibility associated with a 60-fold enhancement of the total scattering cross section (SCS). Besides splitting the EQ and EO modes, broadband ED and MD resonances also contribute to the SCS of the magnetized InSb antenna.

The contribution of the LDOS to the total decay rate of a quantum emitter implies that local electric field enhancement provided by the plasmonic characteristics of the InSb antenna significantly improves the radiative decay rate of an emitter coupled to the antenna. Such a unique feature motivates us to study the dynamic engineering of a dipole emitter's radiative decay rate in microscale proximity to the spherical InSb antenna beyond a quasi-static approximation. In this direction, the InSb antenna is fed by an x-oriented ED source with the coupling distance of $d = 3$ μm. The coupled system balances the divergent effects at this distance, avoiding the reduction of the emitter to a plane wave at larger distances and mitigating the dominant non-radiative Forster rate energy transfer (FRET) at closer ranges [23]. The nature and orientation of the emitter also play important roles in coupled system design, enabling the selective excitation of the resonant modes of the antenna [57].

Figures 1(c) and (d) depict the dependence of the radiative decay rate on frequency for the InSb antenna excited by the x-oriented ED source. Without the magnetic field, as shown in figure 1(c), the radiative decay rate witnesses a significant enhancement in the frequency range from $\omega/\omega_p = 0.9$ to 0.95, corresponding to the spectral interval of the parent EQ and EO resonances. The radiative decay rate experiences approximately 200-fold enhancement due to the EO resonance with a high Q-factor, while a broader EQ resonance leads to a lower enhancement. On the other hand, the magnetized coupled system realizes multi-band radiative decay rate enhancement owing to the contribution of Zeeman-splitting EO, EQ, and ED modes to the radiative coupling channels. The mechanisms of the radiative decay rate enhancement around frequencies of $\omega/\omega_p = 0.85$ and 0.925 are similar to the unmagnetized case. Lower Zeeman-splitting EO and EQ modes resonantly interact with the transition moment of the ED source, realizing up to 50-fold radiative decay rate enhancement at $\omega/\omega_p = 0.85$. As shown in figure 1(c), another enhancement arises from the EO and EQ modes at $\omega/\omega_p = 0.925$, where the latter broadens the spectral response of the radiative decay rate. Another maximum radiative decay rate is also observed at $\omega/\omega_p = 0.98$, resulting from the higher Zeeman-splitting EO resonance.

An interesting behavior of the magnetized InSb antenna is observed in figure 1(d), where the radiative decay rate enhances up to 60 times due to the resonant interaction of the ED source's transition moment with both the broad EQ and higher Zeeman-splitting EO modes. However, without the magnetic field, the InSb antenna is invisible; thus, the radiative decay rate equals one across the spectral range highlighted by the gray area. As mentioned earlier, the antenna can dissipate the emitted energy of the ED source either radiatively or non-radiatively. In the coupled emitter-antenna system, the radiative decay rate channel corresponds to the antenna's scattered electromagnetic field at the emitter position. In contrast, the non-radiative decay rate channel is proportional to the absorption losses of the antenna.

As mentioned earlier, the coupling distance (d) is another crucial parameter modifying the total decay rate. Figures 1(e) and (f) indicates the distance dependence of the radiative and non-radiative decay rates at the fixed frequency of $\omega/\omega_p = 1.05$ associated with the transparent window of the InSb antenna. Under zero magnetization, the radiative decay rate is unity, irrespective of the coupling distance, since the antenna is invisible and the surrounding electromagnetic environment evokes free space for the dipole source. By applying the static magnetic field $B_z = 0.2$ T, Zeeman-splitting modes realize a 60-fold enhancement for the radiative decay rate when the ED source and the antenna are in close proximity. By increasing the coupling distance, the resonant interaction of splitting modes with the ED source's transition moment weakens, and thus the enhancement factor decreases. For longer distances, the enhancement factor is unity as the dipole

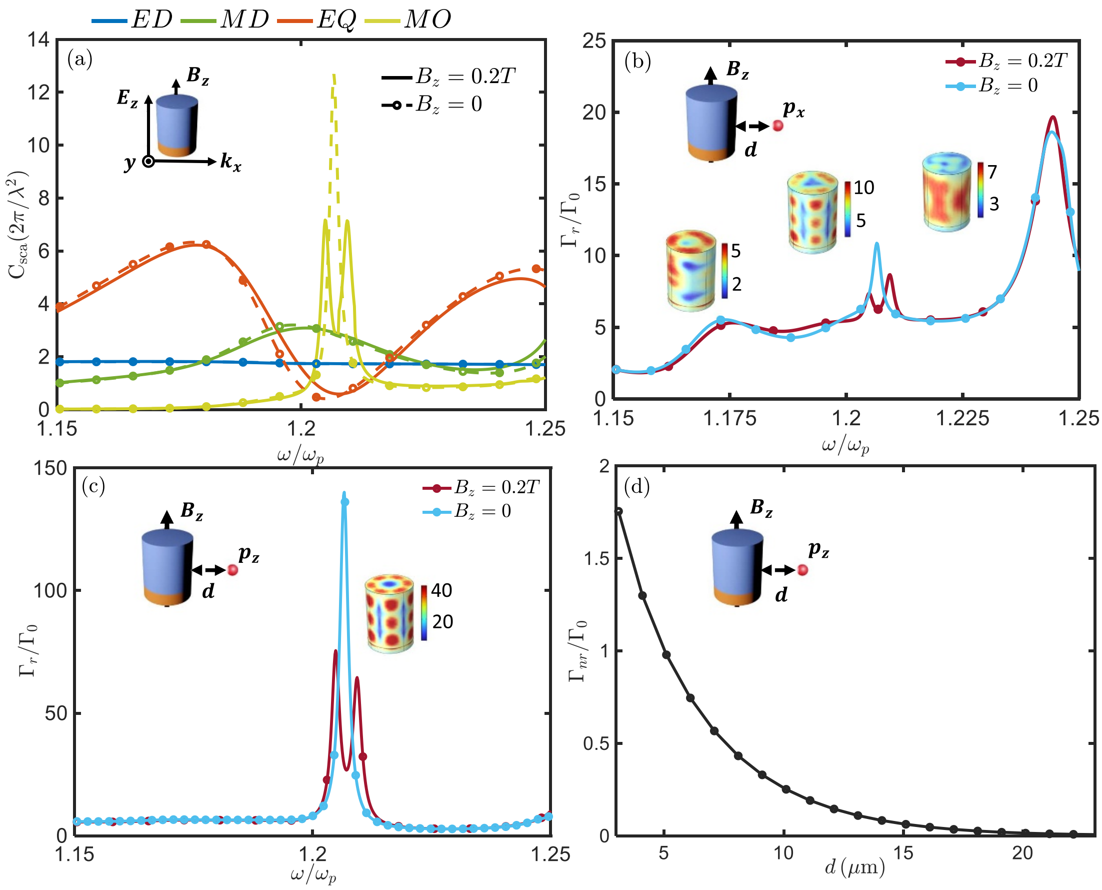

Figure 2. (a) The scattering spectra of the hybrid antenna under plane-wave illumination in the static magnetic field's presence (solid lines) and absence (dashed lines). By applying the static magnetic field ($B_z = 0.2$ T) along the z-direction, multipole moments experience a slight redshift due to the Zeeman effect, while the high-Q parent MO mode splits into two resonant modes in the spectral interval from $\omega/\omega_p = 1.2$ to 1.22. (b) The enhancement of the radiative decay rate for the coupled system is driven by an x-oriented ED emitter as a function of frequency. In this orientation, every multipole moment contributes radiatively to the coupling channels. The insets, showing the normalized electric-field distributions for each resonance peak, highlight the relatively weak coupling between the multipole moments and the ED source. (c) The radiative decay rate of the z-oriented ED source located near the hybrid antenna with the coupling distance of $d = 3\ \mu$m. The spectral response of the radiative decay rate demonstrates a strong dual-band enhancement factor upon magnetization, whereas the maximum radiative decay rate enhancement is recorded under zero magnetic bias. The insets display the normalized electric-field distribution of the MO resonance peak excited by the ED emitter. (d) The non-radiative decay rate of the magnetized system versus coupling distance upon the z-oriented ED emitter excitation at the fixed frequency of $\omega/\omega_p = 1.205$ corresponding to the resonance frequency of the MO mode.

source cannot 'feel' the antenna (see figure 1(e)). As shown in figure 1(f), the unmagnetized coupled emitter-antenna experiences a zero non-radiative decay rate due to the invisibility of the antenna. Under a biased magnetic field of $B_z = 0.2$ T, a strong near-field interaction between the ED source's transition moment and the broad ED mode of the antenna dramatically enhances the non-radiative decay rate for shorter coupling distances due to FRET phenomena. This non-radiative dipole-dipole interaction becomes ineffective for longer coupling distances, so the non-radiative decay rate falls to zero far from the antenna (see figure 1(f)). The magnetized InSb antenna is an active photonic device that allows us to realize dynamic tunable multi-band SE rate enhancement. However, the total emitted power of the ED source is mainly absorbed by the antenna in the near-field region due to significant Joule heating losses of the InSb material, as shown in figure 1(f). Dominant non-radiative channels in the coupled system design give rise to a low quantum efficiency for the antenna, impairing the high free-space radiation rate required for SPSs. We propose an all-dielectric antenna featuring a high quantum efficiency in the following.

3.2. Hybrid Si-InSb antenna

Let us consider a hybrid cylindrical antenna composed of silicon (Si) and InSb layers with the same radii of $r = 35\ \mu$m in the THz regime (depicted in figure 2). The Si layer, as a high-index and low-loss material, comprises the antenna's upper part with a height of $h_1 = 80\ \mu$m to harness the Joule heating losses of the design. The dielectric permittivity of Si is set to $\varepsilon_{Si} = 10.6$ since the material shows a constant permittivity with negligible inherent losses in the studied frequency range. The lower part is made of InSb with a height of $h_2 = 8\ \mu$m to supply the magneto-optical properties required for this active antenna. The design principle resides in two aspects. First, the aspect ratio, $(h_1 + h_2)/r$, of the cylindrical antenna is optimized to support scattering resonances with high Q factors [58]. Second, a given spectral range far from the main absorption band of InSb is chosen such that the material shows moderate positive dielectric permittivity and low losses, as shown in figure S1. When both constituent elements of the antenna exhibit dielectric behaviors, an induced displacement current exceeds the conductive one in the desired frequency range, and thus the all-dielectric antenna can excite robust concurrent electric and magnetic resonances (See figure S3).

In figure 2, we investigate the radiative decay rate variations of an emitter with ED transition near the hybrid antenna with the coupling distance of $d = 3\ \mu$m. We show the SCS of the cylindrical antenna under plane-wave illumination in figure 2(a). In the presence of a magnetic field $B_z = 0.2$ T, a dominant narrow linewidth magnetic octupole (MO) mode is split into distinct resonances due to the Zeeman effect, while the other broadband multipole resonances experience slight blue-shifts. Two MO resonances at frequencies of $\omega_{-,MO}/\omega_p = 1.202$ and $\omega_{+,MO}/\omega_p = 1.206$ result from a parent MO resonance at $\omega/\omega_p = 1.204$. Positioning the x-oriented ED source perpendicular to the hybrid antenna's nearest surface, specifically at the side, enhances the radiative decay rate by a factor of 20 around $\omega/\omega_p = 1.24$, due to the strong contribution from the broad EQ mode to the radiative coupling channels. In this configuration, the high-Q MO mode has only weak coupling with the emitter, resulting in a more modest, 10-fold enhancement of the radiative factor around the resonance frequency of the MO mode (see figure 2(b)).

Under a magnetic bias $B_z = 0.2$ T, the coupled system retains multi-band radiative decay rate enhancement, akin to the unmagnetized case. However, the contribution of the MO splitting modes to the radiative coupling channels undergoes further attenuation due to the Zeeman effect.

Considering the significant impact of the emitter's orientation on decay-rate enhancement, we examine a configuration in which a z-oriented ED emitter is aligned parallel to the incident polarization and situated at the side position relative to the antenna, as illustrated in figure 2(c). Under zero magnetization, the MO mode strongly contributes to the radiative coupling channels, and the radiative decay rate experiences up to a 140-fold enhancement. As shown in figure 2(c), the coupled system can enhance the dual-band radiative decay rate when the magnetized antenna supports the MO splitting resonances. The insets display the normalized electric field distributions of the coupled system, allowing us to perceive the contribution of multipole moments in the coupling channels. In figure figure 2(b), the emitter is oriented perpendicularly to the antenna's surface and the incident electric field, predominantly stimulates the electric multipolar resonances. In contrast, figure 2(c) shows that an emitter parallel to the antenna's surface and the incident electric field tends to couple more effectively with the magnetic multipolar resonances.

Figure 2(d) depicts the non-radiative decay rate of the z-oriented ED source as a function of the coupling distance (d), highlighting that the power absorbed by the antenna at the MO mode's resonance frequency, corresponding to the maximum radiative decay rate, is negligible. This verifies the superior performance of the proposed all-dielectric antenna in minimizing dissipative losses compared to plasmonic coupled systems, demonstrated by the significantly reduced non-radiative decay rate relative to the radiative decay rate in the near-field region. As demonstrated in figure 2, a magnetic hotspot is achieved due to the MO resonance with a high Q factor, promising highly efficient control of the radiative decay rate of an MD emitter.

An x-oriented MD emitter, located perpendicular to the closest surface of the antenna, enables the strong radiative coupling channels with the MO resonant modes in the spectral range from $\omega/\omega_p = 1.2$ to 1.21. In the coupled MD emitter-antenna system, the radiative decay rate demonstrates a 600-fold enhancement due to a narrow-linewidth MO resonance under a zero-bias magnetic field that can be engineered in the presence of the applied magnetic field (See figure 3(a)). Hence, selective emission is another promising advantage of the magnetized hybrid antenna in which spectral bands of the enhanced radiative decay highly depend on the applied magnetic field's strength. Increasing the applied magnetic field makes resonance peaks well-separated across a broader spectral range. The Zeeman-splitting effect is linearly proportional to the cyclotron frequency for magnetic fields $B_z < 0.3$ T, and the split lines are symmetrical to the original resonance peak observed at $B_z = 0$. Based on Bohr magneton approximation, we cannot estimate the spectral position of splitting resonances for larger magnetic field values. New resonance peaks are asymmetrically separated compared to the original resonance. As demonstrated in figure 3(b), higher-frequency splitting

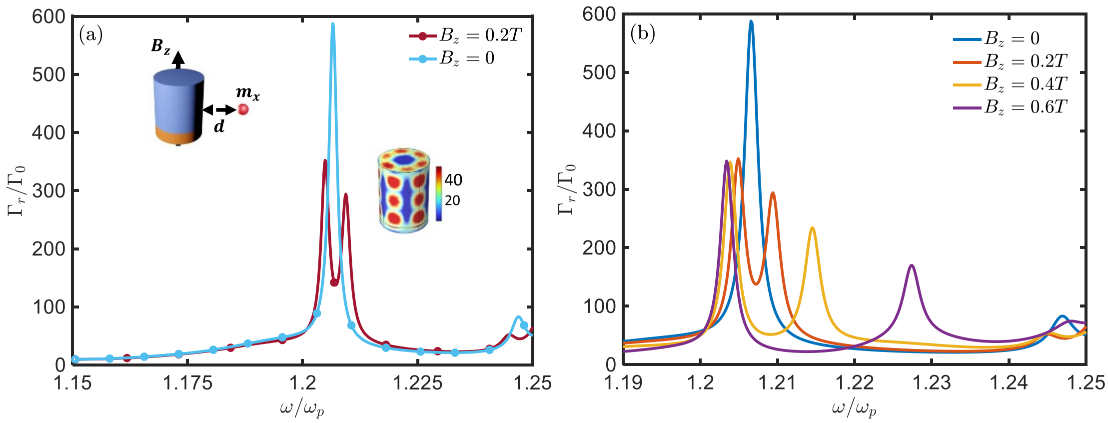

Figure 3. (a) Frequency-dependent radiative decay rate of the x-oriented MD emitter positioned near the hybrid antenna. The high-Q MO resonance generates substantial radiative coupling with the emitter's transition MD moment, leading to a 600-fold enhancement in the photon production rate (b). Dynamically tunable dual-band radiative decay rate enhancement of the x-oriented MD source employing the applied magnetic field increment in the frequency range corresponding to the high-Q MO mode.

resonances experience considerable blue-shifts while lower ones are slightly red-shifted under a biased magnetic field $B_z > 0.3$ T.

3.3. Optimized coupled system design

As highlighted previously, the normalized total decay rate depends on the position, orientation, and type of the dipole source or quantum emitter. Evaluating decay rates based on varied antenna parameters presents complexity and labor intensiveness such that numerical and semi-analytical methods often ignore mutual interactions, leading to suboptimal results. To address this challenge, we employ advanced deep-learning methods recognized for navigating complex and multi-dimensional datasets. We propose a convolutional neural network (CNN) architecture to discern spatial intricacies within the coupled emitter-antenna system. This CNN design adopts several convolutional layers, employing rectified linear unit (ReLU) activation to determine hierarchical data representations. CNN output undergoes flattening and feeds into dense layers for predictive analysis.

As illustrated in figure 4(a), the CNN inputs encompass the spatial coordinates of the quantum emitter, the operational frequency, the value of the applied static magnetic field, and the type of quantum emitter. The initial computational step involves the convolution layer of $C_i = \mathrm{ReLU}(\mathrm{Conv}(X, W_i) + b_i)$, where C_i determines each layer output. Here, X represents the input data, W_i is the weight matrix for the ith filter and b_i is its corresponding bias. The ReLU function introduces non-linearity, allowing the model to adjust its prediction. This operation is repeated for $i = 1$ to N, where N is the total number of filters in the convolution layer.

The output is passed through fully connected layers, and the network undergoes a flattening process, converting the 2D data structure from the convolution layer into a 1D vector. This process of transformation is represented as $\mathrm{FC} = \mathrm{ReLU}(W_{\mathrm{FC}} \times \mathrm{Flatten}(C_N) + b_{\mathrm{FC}})$, where W_{FC} represents the weight matrix and b_{FC} is the bias for the fully connected layers. The network concludes with the output layer, which uses the expression of $\hat{Y} = W_{\mathrm{out}} \times \mathrm{FC} + b_{\mathrm{out}}$, where the output $\hat{Y}$ demonstrates the estimated radiative or non-radiative decay rate.

Utilizing our approach, we can determine both the type and optimal positioning of a quantum emitter near an antenna to optimize radiative decay rates. Figure 4(b) illustrates the radiative decay rate for a dipole source positioned variably around the antenna's external surface. Notably, an x-oriented MD source placed adjacent to the hybrid antenna at $(37\,\mu\mathrm{m}, 0\,\mu\mathrm{m}, 40\,\mu\mathrm{m})$ reaches an enhancement factor of 700 at the frequency range corresponding to the MO mode's resonance frequency under zero magnetization. To verify this prediction, figure 4(c) displays the simulation result of both radiative and non-radiative decay rates for m_x dipole source at its prime location, mirroring CNN's predictive output. The inset presents the far-field radiation pattern of the maximum value corresponding to the dominant MO mode in a non-magnetized state.

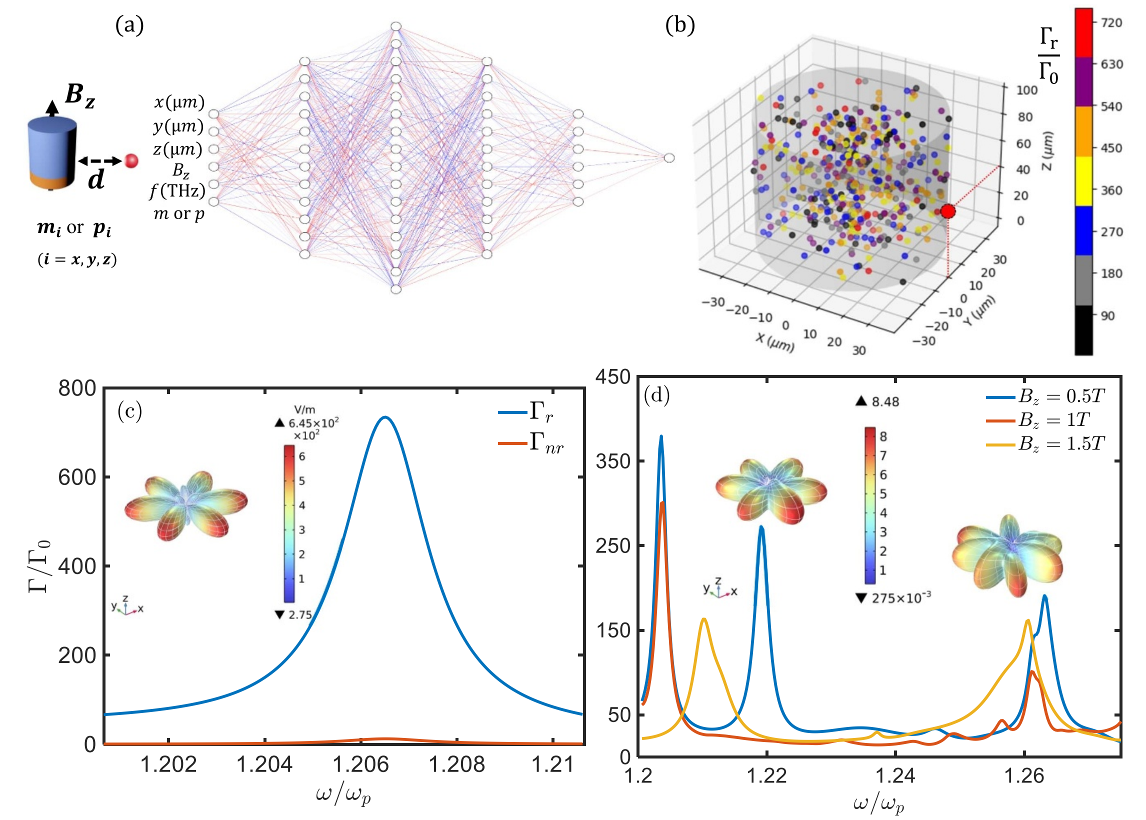

Figure 4. (a) The CNN architecture is tailored to identify the ideal position of a variably oriented dipole source that yields the maximum radiative decay rate near the hybrid antenna. This approach holds the constant coupling distance ($d = 3\,\mu$m). (b) The radiative decay rate of the m_x dipole source at varied positions around the hybrid antenna's outer surface. The CNN prediction indicates a seven-fold enhancement factor when m_x is situated at ($37\,\mu$m, $0\,\mu$m, $40\,\mu$m) within the frequency range corresponding to the MO mode in a non-magnetized state (c). The radiative and non-radiative decay rates of the m_x dipole source at its optimal position align with the MO mode's resonant frequency in a non-magnetized environment under numerical simulation. The maximum value of the radiative decay rate validates the CNN prediction. The inset highlights the far-field radiation pattern, emphasizing the dominant radiation efficiency of the MO mode in free space. (d) The radiative decay rate variations for three different values of the applied magnetic field. The Zeeman-splitting effect becomes broader with the increment in the applied magnetic field, while the enhancement factor decreases compared to the absence of the magnetic field. The insets display the spatial variations of the far-field electric-field patterns corresponding to radiative decay rate maxima at the resonant frequencies of $\omega/\omega_p = 1.207 (B_z = 1.5\,\text{T})$ and $\omega/\omega_p = 1.264$ ($B_z = 1\,$T).

4. Conclusions

In this study, we numerically investigated the impact of an active antenna on the total decay rate of an emitter. The active antenna allows one to dynamically manipulate the scattering response by external agents. InSb material, a III-V semiconductor with strong magneto-optical properties in the THz region, has been employed to realize the active antenna that can modify light–matter interaction via an applied static magnetic field. We used the multipole decomposition method to obtain the SCS of the antenna under plane-wave illumination. The scattering response of the antenna allows us to determine which type of emitters efficiently interact with the antenna.

In the first section, we proposed a spherical InSb antenna to modify the radiative decay rate of an ED source upon magnetization. We have shown that the radiative decay rate experiences a multi-band enhancement when the magnetized antenna has plasmonic features. In contrast, the maximum enhancement factor of about 200 times is observed for the unmagnetized case. Moreover, a transition from invisibility to visibility has been shown in the ENZ region such that the transparent antenna turns into a strong scatterer under a biased magnetic field. Thus, the radiative decay rate dramatically increases by up to 60 times. However, the proposed active antenna suffers from high Joule heating losses, impairing its quantum efficiency associated with a low photon production rate.

To mitigate this limitation, we proposed a cylindrical hybrid antenna composed of Si and InSb layers to act as an all-dielectric active antenna. Due to its robust magnetic resonance, we have found that the hybrid antenna is very promising for dynamic control of the radiative decay rate of an MD emitter. Results show that the magnetized hybrid antenna achieves an enhanced tunable dual-band radiative decay rate for the MD source, so each band represents enhancement factors of several hundred. Moreover, we have found that the hybrid antenna harnesses non-radiative processes, leading to high quantum efficiency.

Finally, we employed a modified deep-learning CNN to determine the emitter's position within the coupled system precisely. This position maximizes the radiative decay rate when an x-oriented MD source, located at the coordinates $(37\ \mu\mathrm{m}, 0\ \mu\mathrm{m}, 40\ \mu\mathrm{m})$, couples with the hybrid antenna. Remarkably, this configuration boosts the radiative decay rate up to 720 times under zero magnetization. This finding was further validated through numerical simulations using Comsol, confirming the prediction of our modified deep-learning network. Offering dynamic splitting bandwidth via the proposed coupled system holds significant potential for designing tunable THz SPSs suitable for practical quantum applications.

Data availability statement

All data that support the findings of this study are included within the article (and any supplementary files).

ORCID iDs

Sina Aghili https://orcid.org/0009-0006-9641-4241
Carsten Rockstuhl https://orcid.org/0000-0002-5868-0526

References

[1] Drexhage K H 1970 Influence of a dielectric interface on fluorescence decay time *J. Lumin.* **1** 693–701
[2] Purcell E M, Cutler Torrey H and Pound R V 1946 Resonance absorption by nuclear magnetic moments in a solid *Phys. Rev.* **69** 37
[3] Glauber R J and Lewenstein M 1991 Quantum optics of dielectric media *Phys. Rev.* A **43** 467
[4] Paesani S, Borghi M, Signorini S, Maïnos A, Pavesi L and Laing A 2020 Near-ideal spontaneous photon sources in silicon quantum photonics *Nat. Commun.* **11** 1–6
[5] Choi S, Tran T T, Elbadawi C, Lobo C, Wang X, Juodkazis S, Seniutinas G, Toth M and Aharonovich I 2016 Engineering and localization of quantum emitters in large hexagonal boron nitride layers *ACS Appl. Mater. Interfaces* **8** 29642–8
[6] Wang R, Ikezawa M, Sakuma Y, Takeda H, Ikeda N, Sugimoto Y, Sakoda K, Yamada Y and Masumoto Y 2020 Enhanced spontaneous emission rates for single isoelectronic luminescence centers in photonic crystal cavities *ACS Photonics* **7** 321–6
[7] Arbel D, Berkovitch N, Nevet A, Peer A, Cohen S, Ritter D and Orenstein M 2011 Light emission rate enhancement from inp MQW by plasmon nano-antenna arrays *Opt. Express* **19** 9807–13
[8] Romeira B and Fiore A 2018 Purcell effect in the stimulated and spontaneous emission rates of nanoscale semiconductor lasers *IEEE J. Quantum Electron.* **54** 1–12
[9] Wang F, Jin S, Sun W, Lin J, You B, Li Y, Zhang B, Hayat T, Alsaedi A and Tan Z' 2018 Enhancing the performance of blue quantum dots light-emitting diodes through interface engineering with deoxyribonucleic acid *Adv. Opt. Mater.* **6** 1800578
[10] Peng Y, Li Z, Tongwei W, Wang Y-T, Tong X, Chuan-Feng Li, Wang Z, Wei S-H, Zhang Y and Liu H 2019 Nanowire quantum dot surface engineering for high temperature single photon emission *ACS Nano* **13** 13492–500
[11] Russell K J, Liu T-L, Cui S and Evelyn L H 2012 Large spontaneous emission enhancement in plasmonic nanocavities *Nat. Photon.* **6** 459–62
[12] Tam F, Goodrich G P, Johnson B R and Halas N J 2007 Plasmonic enhancement of molecular fluorescence *Nano Lett.* **7** 496–501
[13] Cambiasso J, Grinblat G, Li Y, Rakovich A, Cortés E and Maier S A 2017 Bridging the gap between dielectric nanophotonics and the visible regime with effectively lossless gallium phosphide antennas *Nano Lett.* **17** 1219–25
[14] Aharonovich I, Englund D and Toth M 2016 Solid-state single-photon emitters *Nat. Photon.* **10** 631–41
[15] Buckley S and Rivoire K J 2012 Engineered quantum dot single-photon sources *Rep. Prog. Phys.* **75** 126503
[16] Alexander Lohrmann A, Johnson B C, McCallum and J C and Castelletto 2017 A review on single photon sources in silicon carbide *Rep. Prog. Phys.* **80** 034502
[17] Purcell E M 1995 Spontaneous emission probabilities at radio frequencies *Confined Electrons and Photons* (Springer) pp 839–839
[18] Haroche S, Raimond J-M and Dowling J P 2014 Exploring the quantum: atoms, cavities and photons *Am. J. Phys.* **82** 86–87
[19] Qian Z, Shan L, Zhang X, Liu Q, Yun M, Gong Q and Ying G 2021 Spontaneous emission in micro-or nanophotonic structures *PhotoniX* **2** 1–35
[20] Inam F A, Ahmed N, Steel M J and Castelletto S 2018 Hyperbolic metamaterial resonator–antenna scheme for large, broadband emission enhancement and single-photon collection *J. Opt. Soc. Am.* B **35** 2153–62
[21] Ahmed N, Akhtar S and Inam F A 2020 Hyperbolic metamaterial-based metal–dielectric resonator-antenna designs for GHZ photon collection rates from wide-range solid-state single-photon sources *J. Opt. Soc. Am.* B **37** 3469–77
[22] Guclu C, Shan Luk T, Wang G T and Capolino F 2014 Radiative emission enhancement using nano-antennas made of hyperbolic metamaterial resonators *Appl. Phys. Lett.* **105** 123101
[23] Bonod N 2020 Controlling spontaneous emission with dielectric optical antennas *Dielectric Metamaterials* (Elsevier) pp 109–44
[24] Agio M 2012 Optical antennas as nanoscale resonators *Nanoscale* **4** 692–706
[25] Taminiau T H, Stefani F D, Segerink F B and Van Hulst N F 2008 Optical antennas direct single-molecule emission *Nat. Photon.* **2** 234–7
[26] Cui L, Zhu Y, Abbasi M, Ahmadivand A, Gerislioglu B, Nordlander P and Natelson D 2020 Electrically driven hot-carrier generation and above-threshold light emission in plasmonic tunnel junctions *Nano Lett.* **20** 6067–75
[27] Anger P, Bharadwaj P and Novotny L 2006 Enhancement and quenching of single-molecule fluorescence *Phys. Rev. Lett.* **96** 113002
[28] Hua Mi, Wang L, Zhang Y, Zhao G and Jiang R 2019 Control of the emission from electric and magnetic dipoles by gold nanocup antennas *Opt. Express* **27** 14221–30
[29] Jiang Q, Roy P, Claude J-Bit and Wenger Jome 2021 Single photon source from a nanoantenna-trapped single quantum dot *Nano Lett.* **21** 7030–6

[30] Aghili S, Golmohammadi S and Amini A 2018 Proposing an on/off optical router in telecom wavelength using plasmonic tweezer *Opt. Commun.* **427** 95–100

[31] Rogobete L, Kaminski F, Agio M and Sandoghdar V 2007 Design of plasmonic nanoantennae for enhancing spontaneous emission *Opt. Lett.* **32** 1623–5

[32] Hein S M and Giessen H 2013 Tailoring magnetic dipole emission with plasmonic split-ring resonators *Phys. Rev. Lett.* **111** 026803

[33] Dhawan A R *et al* 2020 Extreme multiexciton emission from deterministically assembled single-emitter subwavelength plasmonic patch antennas *Light: Sci. Appl.* **9** 1–9

[34] Dmitriev P A, Baranov D G, Milichko V A, Makarov S V, Mukhin I S, Samusev A K, Krasnok A E, Belov P A and Kivshar Y S 2016 Resonant Raman scattering from silicon nanoparticles enhanced by magnetic response *Nanoscale* **8** 9721–6

[35] Iwanaga M 2018 All-dielectric metasurfaces with high-fluorescence-enhancing capability *Appl. Sci.* **8** 1328

[36] Cheng L, Alaee R, Safari A, Karimi M, Zhang L and Boyd R W 2021 Superscattering, superabsorption and nonreciprocity in nonlinear antennas *ACS Photonics* **8** 585–91

[37] Mobini E, Alaee R, Boyd R W and Dolgaleva K 2021 Giant asymmetric second-harmonic generation in bianisotropic metasurfaces based on bound states in the continuum *ACS Photonics* **8** 3234–40

[38] Liu S, Vaskin A, Campione S, Wolf O, Sinclair M B, Reno J, Keeler G A, Staude I and Brener I 2017 Huygens metasurfaces enabled by magnetic dipole resonance tuning in split dielectric nanoresonators *Nano Lett.* **17** 4297–303

[39] Yang Y, Zhu B and Dai H 2020 Strong magnetic field enhancement and magnetic purcell effect in a dielectric disk-ring composite nanocavity *J. Opt. Soc. Am.* B **37** 702–8

[40] Rolly B, Bebey B, Bidault S, Stout B and Bonod N 2012 Promoting magnetic dipolar transition in trivalent lanthanide ions with lossless mie resonances *Phys. Rev.* B **85** 245432

[41] Elli Stamatopoulou P and Tserkezis C 2021 Role of emitter position and orientation on silicon nanoparticle-enhanced fluorescence *OSA Continuum* **4** 918–32

[42] Chew H 1987 Transition rates of atoms near spherical surfaces *J. Chem. Phys.* **87** 1355–60

[43] Aslan E 2021 Engineering of dual-band magnetic dipole decay rate enhancement with concentric hollow nanodisk resonators *Opt. Mater.* **113** 110871

[44] Filonov D S, Krasnok A E, Slobozhanyuk A P, Kapitanova P V, Nenasheva E A, Kivshar Y S and Belov P A 2012 Experimental verification of the concept of all-dielectric nanoantennas *Appl. Phys. Lett.* **100** 201113

[45] Krasnok A, Glybovski S, Petrov M, Makarov S, Savelev R, Belov P, Simovski C and Kivshar Y 2016 Demonstration of the enhanced purcell factor in all-dielectric structures *Appl. Phys. Lett.* **108** 211105

[46] Rocco D, Lamprianidis A, Miroshnichenko A E and De Angelis C 2020 Giant electric and magnetic purcell factor in dielectric oligomers *J. Opt. Soc. Am.* B **37** 2738–44

[47] Zouros G P, Kolezas G D, Almpanis E and Tsakmakidis K L 2021 Three-dimensional giant invisibility to superscattering enhancement induced by zeeman-split modes *ACS Photonics* **8** 1407–12

[48] Chochol J, Postava K, Čada M, Vanwolleghem M, Halagačka L, Lampin J-F and Pištora J 2016 Magneto-optical properties of insb for terahertz applications *AIP Adv.* **6** 115021

[49] Liu W, Chang A Y, Schaller R D and Talapin D V 2012 Colloidal insb nanocrystals *J. Am. Chem. Soc.* **134** 20258–61

[50] Pandya S G and Kordesch M E 2015 Characterization of insb nanoparticles synthesized using inert gas condensation *Nanoscale Res. Lett.* **10** 1–7

[51] Novotny L and Hecht B 2012 *Principles of Nano-Optics* (Cambridge University Press)

[52] Alhalaby H, Zaraket H and Principe M 2021 Enhanced photoluminescence with dielectric nanostructures: a review *Results Opt.* **3** 100073

[53] Comsol Software (available at: www.comsol.com) (Accessed 19 May 2024)

[54] Chen Y, Nielsen T R, Gregersen N, Lodahl P and Mørk J 2010 Finite-element modeling of spontaneous emission of a quantum emitter at nanoscale proximity to plasmonic waveguides *Phys. Rev.* B **81** 125431

[55] Márquez A and Sirvent R E 2020 Terahertz response of plasmonic nanoparticles: plasmonic Zeeman effect *Opt. Express* **28** 39005–16

[56] Alaee R, Rockstuhl C and Corbaton I F 2018 An electromagnetic multipole expansion beyond the long-wavelength approximation *Opt. Commun.* **407** 17–21

[57] Schmidt M K, Esteban R, Sáenz J J, Suárez-Lacalle I, Mackowski S and Aizpurua J 2012 Dielectric antennas-a suitable platform for controlling magnetic dipolar emission *Opt. Express* **20** 13636–50

[58] Rybin M V, Koshelev K L, Sadrieva Z F, Samusev K B, Bogdanov A A, Limonov M F and Kivshar Y S 2017 High-q supercavity modes in subwavelength dielectric resonators *Phys. Rev. Lett.* **119** 243901